Environmental Effects on the Stellar Mass Function in a $z \sim 3.3$ Overdensity of Galaxies in the COSMOS Field

Ben Forrest,[1,2]$\star$ Brian Lemaux,[1,3] Lori Lubin,[3] C3VO, MAGAZ3NE, VUDS

[1]*Department of Physics and Astronomy, University of California Davis, One Shields Avenue, Davis, CA, 95616, USA*
[2]*Department of Physics & Astronomy, University of California Riverside, 900 University Ave., Riverside, CA, 92521, USA*
[3]*Gemini Observatory, NSF's NOIRLab, 670 N. A'ohoku Place, Hilo, HI, 96720, USA*

ABSTRACT

We present an analysis of the number density of galaxies as a function of stellar mass (*i.e.,* the stellar mass function, SMF) in the COSMOS field at $z \sim 3.3$, making a comparison between the SMF in overdense environments and the SMF in the coeval field. In particular, this region contains the overdense Elentári structure, a system of 6 extended overdensities spanning ~ 70 cMpc on a side. A clear difference is seen in the high-mass slope of these SMFs, with overdense regions showing an increase in the ratio of high-mass galaxies to low-mass galaxies relative to the field, indicating a more rapid build-up of stellar mass in overdense environments. This result qualitatively agrees with analyses of clusters at $z \sim 1$, though the differences between protocluster and field SMFs at $z \sim 3.3$ are smaller. In fact, when taking the ratio of the the overdense and field SMFs, similar results are seen at regions of similar quantitative overdensity at both $z \sim 3.3$ and $z \sim 1$. While this is consistent with overdensities enhancing the evolution of their member galaxies, potentially through increased merger rates, whether this enhancement begins in protocluster environments or even earlier in group environments is still unclear. That said, the fractions of quiescent galaxies between the field and overdense environments do not vary significantly, implying that this stellar mass enhancement is ongoing and any starbursts triggered by merger activity have not yet quenched. If mergers are indeed responsible, high resolution imaging of Elentári and similar structures at these early epochs should then reveal increased merger rates relative to the field. Larger samples of well-characterized overdensities are necessary to draw broader conclusions in these areas.

Key words: galaxies: evolution – galaxies: clusters:general

1 INTRODUCTION

The environment in which a galaxy resides plays an important role in its evolution. Obvious differences exist in the local universe between the populations of galaxies in massive, evolved clusters and populations of galaxies in the field across a wide range of properties including stellar mass, star formation rate, age, color, morphology, velocity dispersion, metallicity (*e.g.,* Dressler 1984; Kauffmann et al. 2004; Thomas et al. 2005). These differences are consistent with cluster galaxies having a faster and/or earlier evolutionary timescale than field galaxies and this signal is seen in the most overdense environments out past $z \gtrsim 1$ (*e.g.,* Kawinwanichakij et al. 2017; Papovich et al. 2018), though the strength of this signal begins to decrease or perhaps reverse by $z \gtrsim 1.5$ (Tran et al. 2010; Nantais et al. 2016). In fact, at very early epochs, many galaxies in protoclusters, the progenitors of today's clusters, appear to have enhanced star formation rates (SFRs) relative to the field (*e.g.,* Capak et al. 2011; Hatch et al.

2011; Wang et al. 2016, P. Staab, et al., submitted), suggesting that the effect of an overdense environment is to increase SFRs at early times. This may subsequently deplete the molecular gas content of these galaxies, as seen in low redshift galaxies (*e.g.,* Fumagalli et al. 2009), thus inhibiting future star formation and leaving the galaxy more massive and older than galaxies which continue forming stars. However, the presence of molecular gas reservoirs in $z > 1$ clusters (*e.g.,* Noble et al. 2018) makes this picture less certain. The specific physical mechanisms responsible for any such environmental effects to take place and whether there is a particular density threshold or timescale required for these effects is also unclear.

The combined effects of these processes can be seen by analyzing the number density of galaxies as a function of stellar mass (stellar mass function, SMF). The shape of the SMF between galaxies in clusters and in the field varies significantly, with galaxies in overdense regions showing a larger ratio of high-mass to low-mass galaxies (*e.g.,* Blanton & Moustakas 2009). Some evidence suggests that this variation in shape may be entirely due to changes in shape and/or normalization of the SMF of red / early-type / quiescent

$\star$ E-mail: bforrest@ucdavis.edu

populations, with the shape of the star-forming galaxy SMF staying relatively similar between field and cluster environments (*e.g.,* Peng et al. 2010), though this is not universally found (*e.g.,* Annunziatella et al. 2014, 2016).

Evidence is mixed as to whether or not this is the case in higher redshift overdensities. Targeted spectroscopic observations of cluster environments at $z \sim 1$ such as those in the ORELSE (Lubin et al. 2009), GCLASS (Muzzin et al. 2012), and GOGREEN (Balogh et al. 2017, 2020) surveys have analyzed stellar mass functions and found differences between cluster and field populations. The results from GCLASS (Van Der Burg et al. 2013) and GOREEN (van der Burg et al. 2020) suggest that these differences are due to changes in the relative fraction of quenched galaxies, however the shapes of the quiescent SMFs in both overdensity and field are statistically the same, as are the shapes of the star-forming SMFs. However, results from ORELSE (Tomczak et al. 2017) instead show evolution of shape in both the quiescent and star-forming SMFs with environmental overdensity.

While SMF analyses of field populations $z > 3$ are numerous (*e.g.,* Marchesini et al. 2009; Stefanon et al. 2015; Marsan et al. 2022; Weaver et al. 2023), similar analyses of overdense environments are lacking. This stems from the difficulty of identification and characterization of high redshift overdensities, which is several-fold. Photometric identification of candidate overdensities at these epochs requires deep multiband imaging, in particular in the near-infrared, in order to identify stellar-mass limited samples of faint galaxies, to infer the location of features such as the Balmer break which aid in constraining photometric redshifts, and to cover the large projected sizes of these structures ($\sim 10 - 15$ comoving Mpc, and in some cases larger; Muldrew et al. 2015; Chiang et al. 2017; Cucciati et al. 2018). The low density contrast of these structures with the coeval field combined with significant photometric red-shift uncertainties means that significant spectroscopic follow-up is also required to obtain precise galaxy redshifts, confirm these structures, and allow for accurate density mapping of the systems and their surroundings.

Exploring whether there are environmental effects on the stellar mass function in protocluster environments at $z > 3$ can lead to increased understanding of the mechanisms in overdense environments which contribute to galaxy evolution. To that end, in this work we build a stellar mass function based on galaxies in the COSMOS field around the Elentári structure at $z \sim 3.3$ (Forrest et al. 2023). To our knowledge, this is the first time such an analysis has been performed at this early epoch and is only possible due to a wealth of deep photometric and spectroscopic data as described in Section 2. We discuss the analysis methodology and results in Section 3 before presenting conclusions (Section 4). Throughout this work we use the AB magnitude system (Oke & Gunn 1983) and assume a ΛCDM cosmology with with $H_0 = 70$ km/s/Mpc, $\Omega_M = 0.3$, and $\Omega_\Lambda = 0.7$.

2   DATA

2.1   Parent Photometric Catalogs

This work relies upon the considerable investment of observing time focused on the COSMOS field (Scoville et al. 2007; Koeke-moer et al. 2007). The ultraviolet, optical, and near-infrared imaging in this field have been compiled most recently in the COSMOS2020

catalogs (Weaver et al. 2022), which contain over 1.5 million sources observed in up to 40 bandpasses over ~ 1.5 deg^2. This includes space-based observations from *GALEX* (ultraviolet; Zamojski et al. 2007), *HST*/ACS (optical; Leauthaud et al. 2007) and *Spitzer*/IRAC (near-infrared Ashby et al. 2013, 2015, 2018; Steinhardt et al. 2014). Ground based data includes ultraviolet CFHT/MegaCam observations (Sawicki et al. 2019), optical data from Subaru/Suprime-Cam (Taniguchi et al. 2007, 2015) and Hyper Suprime-Cam (Aihara et al. 2019), and near-infrared observations from VISTA/VIRCAM (McCracken et al. 2012; Moneti et al. 2019).

The depth of the imaging involved in construction of the COS-MOS2020 catalogs as well as their associated derived properties, including well-characterized photometric redshifts (z_{phot}) and their probability distributions ($p(z)$), rest-frame colors, stellar masses, and SFRs are critical to this work. Unless otherwise stated, we use the COSMOS2020 Classic catalog, and the associated properties derived using `LePhare` (Arnouts et al. 1999; Ilbert et al. 2006). These characterizations use the same process as described in Il-bert et al. (2013), and include galaxy templates from Polletta et al. (2007), Bruzual & Charlot (2003), and Onodera et al. (2012), and stellar templates from Pickles (1998), with additional templates for white and brown dwarfs as well as AGN. Allowed dust attenuation curves include Small Magellanic Cloud (Prevot et al. 1984), starburst (Calzetti et al. 2000), and starburst+2175Å profiles (Fitz-patrick & Massa 1986), and a Chabrier (2003) IMF is assumed.

2.2   Spectroscopy

2.2.1   Field Surveys

The COSMOS field has also been the target of many spectroscopic surveys, several of which are included in this work. The VIMOS Ultra-Deep Survey (VUDS; Le Fèvre et al. 2015), targeted $\sim 10^4$ objects across the COSMOS, ECDFS, and VVDS-2h fields with the VIMOS instrument on ESO-VLT (Le Fèvre et al. 2003). This survey preferentially selected targets for follow-up which had $z_{phot} \gtrsim 2$ and was deep enough to reliably detect continuum for $i \sim 25$ objects.

The zCOSMOS survey (Lilly et al. 2007) also used the VI-MOS spectrograph on the VLT and consisted of two sub-samples. The zCOSMOS-bright subsample targeted $\sim 2 \times 10^4$ galaxies with $I < 22.5$ and thus mainly confirmed galaxies across $0.1 < z < 1.2$ over the entire COSMOS ACS field. The zCOSMOS-deep subsample targeted $\sim 10^4$ galaxies in the central portion of the field believed to have $1.4 < z < 3.0$ based on their colors (Daichi, K. et al., in preparation).

The DEIMOS 10k Spectroscopic Survey (Hasinger et al. 2018) similarly targeted $\sim 10^4$ objects, using the DEIMOS instrument on the Keck II telescope (Faber et al. 2003). While the entirety of this survey was in the COSMOS field, there was no photometric redshift cut applied and thus the majority of objects with spectroscopic redshifts are at $z < 2$.

These surveys have also used similar spectroscopic redshift quality flagging systems. The base flag for each object is one of the following: 0 - no redshift measured, 1 - low confidence redshifts, 2, 3, 4, 9 - secure redshifts (estimated $\gtrsim 75\%$ reliability; Le Fèvre et al. 2013). Each flag may also prepended with a number X, indicating that the target either has broad lines observed in the spectrum (X=1), the target is a serendipitous detection (X=2), or the target is a serendipitous detection at location of target (*i.e.,* chance alignment or merger; X=3).

Table 1. C3VO Keck/MOSFIRE Observations in COSMOS. H-band exposures were 120s each, K-band exposures were 180s each. The slitwidth was 0.7″.

Target	Mask	Bandpass	Date(s) Observed	Exp.Time (m)	Avg. Seeing(″)
Hyperion	Hyperion1	H	2020.03.09	150	0.71
	Hyperion2	H	2020.03.09	112	0.69
	Hyperion3	H	2020.03.10	106	0.66
	Hyperion4	H	2020.03.11	104	0.55
	Hyperion5	H	2020.03.11	106	0.55
	Hyperion6	H	2020.11.30	118	0.79
	Hyperion7	H	2020.11.30	164	0.86
			2021.01.06		
			2021.12.25		
Elentàri	DONGOCps23n24_1	K	2021.12.26	102	0.77
	DONGOCps23n24_2	K	2021.12.26	102	0.68
	DONGOCps23n24_3	K	2022.10.15	48	0.86
	NEb_1	K	2023.02.03	90	0.86
	NEc_1	K	2023.03.30	60	0.67
	NEd_1	K	2023.03.30	42	0.81
	Bridge1	K	2023.02.03	84	0.89
			2023.03.30		
	Bridge2	K	2023.03.31	72	0.70
	SWa_1	K	2023.02.03	84	1.00
			2023.03.30		
	SWc_1	K	2023.03.31	48	0.93

Table 2. C3VO Keck/DEIMOS Observations in COSMOS. The 600ZD grating (600 lines/mm) was used for all observations.

Target	Mask	Filter	Central Wavelength (Å)	Date(s) Observed	Exp.Time (m)	Avg. Seeing(″)
Taralay	dongN1C	GG400	6500	2017.12.26	210	0.8
	dongS1B	GG400	6500	2016.12.22	275	0.8
	dongD1	GG455	7200	2017.12.26	320	0.94
				2019.02.05		
				2019.12.24		
				2020.12.23		
	dongD2	GG455	7200	2020.02.02	360	0.78
				2020.12.10		
				2022.12.23		
	dongA1	GG455	7200	2021.01.17	299	0.84
				2022.01.10		
	dongA2	GG455	7200	2022.01.10	240	0.59
				2022.01.101		
PCl J1000+0200	dongC2D1	GG400	6500	2022.01.11	145	0.82
	dongC2N1	GG400	6500	2020.02.02	309	1.15
	dongC2S1	GG400	6500	2019.02.25	268	0.97
				2020.12.10		
				2020.12.23		
				2021.01.17		

2.2.2 Targeted Surveys - C3VO

The Charting Cluster Construction with VUDS (Le Fèvre et al. 2015) and ORELSE (Lubin et al. 2009) Survey (C3VO; Lemaux et al. 2022) has used the Keck/DEIMOS and Keck/MOSFIRE (McLean et al. 2010, 2012) instruments on the Keck telescopes to follow-up candidate overdensities identified in density maps constructed from a combination of spectroscopic and photometric data across the CFHTLS-D1, ECDFS, and COSMOS fields (see Sections 3.1 and 3.2 for a description of these maps and candidate overdensity identification). The survey has observed ∼ 2000 galaxies across the three fields, approximately half with MOSFIRE and half with DEIMOS. Targeted regions included Hyperion ($z = 2.45$;

Cucciati et al. 2018), PCl J1000+0200 ($z = 2.9$; Cucciati et al. 2014), PCl J0227-0421 ($z = 3.3$; Lemaux et al. 2014; Shen et al. 2021), Elentári ($z = 3.35$; McConachie et al. 2022; Forrest et al. 2023), Smruti ($z = 3.47$; Forrest et al. 2017; Shah et al. 2023), and Taralay ($z = 4.57$; Lemaux et al. 2018; P. Staab et al., submitted).

All C3VO COSMOS observations used in this work are shown in Tables 1 & 2. MOSFIRE masks targeting Hyperion as well as the first three masks targeting Elentári used photometric redshifts and magnitudes from the COSMOS2015 catalog (Laigle et al. 2016) for target selection. Subsequent masks targeting Elentári (observed in 2023) selected objects based on $p(z)$, stellar masses, and rest-frame colors from the COSMOS2020 Classic catalog. DEIMOS masks prioritized targeting star-forming galaxies down to $i_{AB} < 25.3$ with

photometric redshifts near that of the overdensity in question, as detailed in Lemaux et al. (2022).

In this work we focus on density maps constructed from data including VUDS and zCOSMOS spectroscopy, photometry from COSMOS2015 and COSMOS2020, and C3VO spectroscopic data taken prior to fall 2021 (the 2021B semester). Spectroscopic redshifts from other listed masks are still used when determining the location of a galaxy along the line of sight.

2.2.3   Targeted Surveys - MAGAZ3NE

The Massive Ancient Galaxies at $z > 3$ Near-Inrared Survey (MAGAZ3NE; Forrest et al. 2020) has used Keck/MOSFIRE to spectroscopically follow-up ultra-massive galaxies (UMGs; $\log(M_*/M_\odot) > 11$ at $z > 3$) and investigate their environments. It has thus far targeted ~ 1000 galaxies across the UltraVISTA (COSMOS), VIDEO-XMM, and VIDEO-CDFS fields. This survey selected targets in the COSMOS field for follow-up based on observed galaxy spectral energy distributions (SEDs), $p(z)$, stellar masses, and SFRs from the UltraVISTA DR1 and DR3 catalogs (Muzzin et al. 2013, A. Muzzin, private communication).

This paper focuses on a set of six structures at $z \sim 3.3$ named Elentári (Forrest et al. 2023). While it is unlikely that all six will collapse into a single system at $z = 0$, there are multiple pairs of structures which may do so. This system as a whole has over 100 spectroscopically-confirmed members, and the best characterized structure has an estimated $z = 0$ mass of 1.3×10^{14} M$_\odot$. Two of these were spectroscopically confirmed via MAGAZ3NE spectroscopy (McConachie et al. 2022) as they contain UMGs, and the larger region was independently identified and then spectroscopically followed-up with C3VO.

2.2.4   Spectroscopic Data Reduction

Details on the data reduction process and redshift assignment for zCOSMOS (Lilly et al. 2007), VUDS (Le Fèvre et al. 2015), and DEIMOS 10k (Hasinger et al. 2018) data can be found in the publications of those surveys. However, all surveys used a combination of automated initial redshift assignment followed by visual inspection and checking of results.

C3VO MOSFIRE spectra were reduced using the MOSDEF 2D data reduction pipeline (Kriek et al. 2015). MAGAZ3NE MOS-FIRE data, which were initially reduced using the MOSFIRE DRP, were also re-reduced using the MOSDEF pipeline. The MOSDEF pipeline subtracts the sky background noise, masks both cosmic rays and bad pixels, and rectifies each frame. The trace of a star on a science slit is then identified, and the frames are shifted to align this trace between frames, accounting for any drift in telescope pointing. This star also allows for a measurement of atmospheric seeing and throughput. All exposures are then coadded, weighting each according to the seeing and throughput values. A telluric correction and flux calibration are then applied. This process results in a higher SNR 2D-spectrum than produced with the Keck-supported Data Reduction Pipeline (DRP; Version 2018), which is particularly important when targeting the same mask for long periods without realigning due to flexure of the system (Hutchison et al. 2020). Combined with the weighting of individual frames, this method returns spectra with increases in SNR of $\sim 5\%$. The resultant 2D spectrum was collapsed in a narrow range around either the strongest emission line or along the entire wavelength axis for continuum sources. This was fit with a Gaussian which was subsequently used for weighting the 1D spectral extraction (optimal extraction Horne 1986).

C3VO DEIMOS spectra were reduced using a modified version of the spec2D pipeline (Cooper et al. 2012), which performs wavelength fitting, background sky subtraction, and 1D spectral extraction. These modifications are detailed in Lemaux et al. (2019) and include improvements in interpolation over the DEIMOS chip gap, throughput correction, and wavelength solution.

2.2.5   Spectroscopic Redshift Determination

The MOSFIRE spectra were visually inspected to identify galaxies with emission lines. At the redshifts considered in this work, emission lines from Hβ and the [O III]$\lambda\lambda$4959,5007 doublet are the most obvious features and when seen, a model consisting of three Gaussians is used to obtain a spectroscopic redshift. This model has four parameters - the redshift, the amplitudes of Hβ and [O III]λ5007, and the width of the lines. The level of stellar continuum is assumed to be constant over the spectral range of the observations, and is taken to be the weighted average flux outside of regions with emission lines. The amplitude of [O III]λ4959 is fixed to 30% that of [O III]λ5007. In this work we are not concerned with the quantification of line velocity widths, velocity offsets, or any broad line components beyond obtaining a redshift as pertains to MOSFIRE spectra. A small number of galaxies at lower redshifts, which had Hα, [N II]$\lambda\lambda$6548,6584, and [S II]$\lambda\lambda$6718,6733 in the wavelengths probed by the MOSFIRE observations were fit with a similar multi-Gaussian model. Each spectroscopic observation is additionally given a quality flag in the style of the zCOSMOS, VUDS, and DEIMOS10k surveys described above which denotes the confidence in the assigned spectroscopic redshift (see *e.g.,* Le Fèvre et al. 2015; Lemaux et al. 2022, for more details).

The DEIMOS spectra were interactively assigned spectroscopic redshifts by using zspec (Newman et al. 2013) as described in Lemaux et al. (2022). The quality flagging for these data follow a DEEP2 style flag (Newman et al. 2013). Similar to the VUDS flagging system, flags of 3 and 4 represent high quality redshifts. For example, the observation of a single emission line skewed redward indicative of Lyα would result in flag 3, and the observation of multiple spectral features would result in flag 4. Flags of 1 and 2 indicate low confidence redshifts. For consistency with the MOSFIRE data and redshifts from the field surveys, C3VO-DEIMOS objects with a quality flag of 2 are changed to a quality flag of 1 when creating the master spectroscopic catalog (next section).

2.3   Catalog Matching and Remodeling SEDs

While target selection for the various spectroscopic surveys used in this work came from different parent photometric catalogs, we compare the spectroscopic redshifts, sky coordinates, and i- and K-band magnitudes from the spectroscopic survey catalogs to the photometric redshifts, coordinates and magnitudes in the same bandpasses from the COSMOS2020 Classic photometric catalog to find the best match. For galaxies targeted in multiple surveys, only the highest quality flag entry was kept. See Appendix A for more details regarding the matching process. Of the 40008 final combined spectroscopic catalog entries, 37771 (94.4%) have a match in the COSMOS2020 Classic catalog. Additionally, 26676 (66.7%) spectroscopic targets have high quality spectroscopic redshift measurements $0 < z < 7$ (quality flags X2, X3, X4, or X9).

With confirmed redshifts of these galaxies, it is necessary to remodel their physical properties, which will change from those given in COSMOS2020 unless the photometric redshift was identical to the spectroscopic redshift. While there are many programs
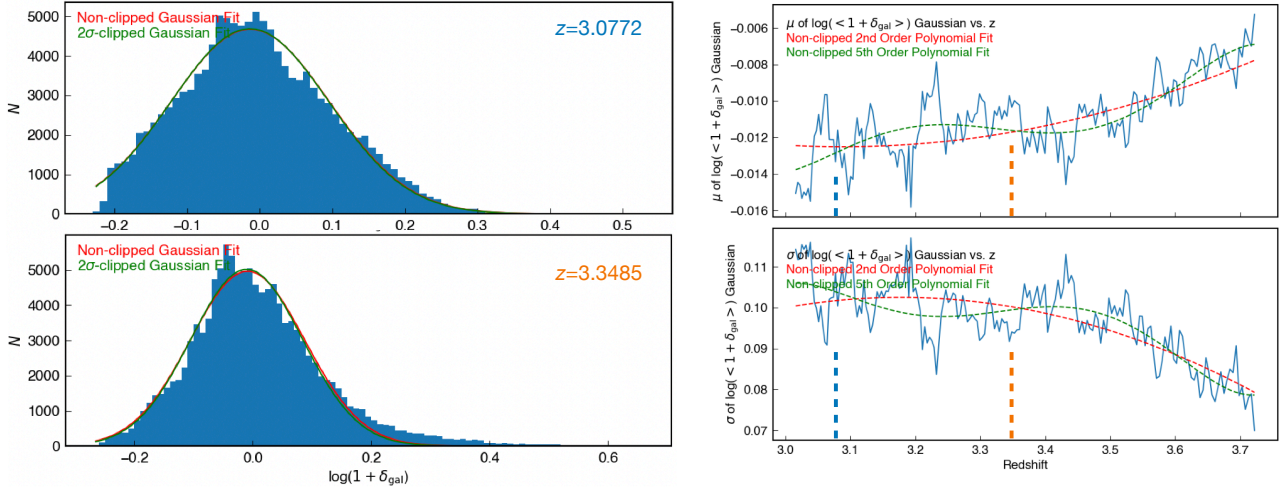
Figure 1. The process for determining the spread in voxel overdensity values for a given redshift slice. **Left:** Histograms of all voxel overdensity values (median set equal to zero) in redshift slices of $z = 3.0772$ (top) and $z = 3.3485$ (bottom). A Gaussian model is fit to the distribution at each slice, which produces a fit mean (μ) and standard deviation (σ). **Right:** The plot of the fit μ (top) and σ (bottom) values for each slice of the VMC map considered in this work. A polynomial is then fit to this distribution to smooth out the effects of any large scale structures on these values, and these polynomial values are used to determine the overdensity significance (σ_δ) of a given voxel. Herein we use the value of a 5th-order polynomial (green), though using a 2nd order polynomial (red) for example does not effect the results.

used to model galaxy spectral energy distributions (SEDs), in this work we use `LePhare` (Arnouts et al. 1999; Ilbert et al. 2006), as this program is used in the COSMOS2020 catalogs. We remodel all spectroscopically confirmed galaxies using the same setup as in COSMOS2020 with the redshift now fixed to the spectroscopic redshift. Detailed descriptions of these choices can be found in the catalog publications above, as well as Ilbert et al. (2009).

As will be described shortly, we also perform a Monte Carlo resampling of the $p(z)$ of galaxies which are not spectroscopically confirmed. For each such galaxy we run `LePhare` with the redshift fixed to values from $3.0 < z < 3.7$ (the redshift range considered in this work) with $\Delta z = 0.05$. The results from this grid are then interpolated to the redshift of a galaxy determined in an individual MC iteration. We found that the differences in the fit stellar mass and star formation rate between adjacent redshift runs for a given galaxy differ by > 0.1 dex in less than 0.3% and 2.3% of cases, respectively, more than sufficient for the studies herein, which validates this interpolation.

3 ANALYSIS

3.1 Voronoi Tesselation Monte Carlo Mapping

We use the Voronoi Tesselation Monte Carlo (VMC) mapping technique to determine galaxy environmental density, a method which has been extensively tested and used to find overdense structures previously (Lemaux et al. 2017; Tomczak et al. 2017; Cucciati et al. 2018; Lemaux et al. 2018; Hung et al. 2020; Shen et al. 2021; Lemaux et al. 2022; Forrest et al. 2023). This method uses a combination of spectroscopic redshifts and photometric redshift probability distributions to statistically determine density in three-dimensional space.

3.1.1 Density maps

Voronoi cells are generated by drawing boundaries that are equidistant from the two nearest galaxies in projected space. This strategy cannot be effectively extended to the redshift dimension due to the uncertain contributions of peculiar velocities for spectroscopically confirmed galaxies and more generally the redshift uncertainties of objects in photometric catalogs. As a result, the volume of interest is divided into redshift slices and only galaxies within such a slice are considered. The slice width is determined from a combination of photometric redshift uncertainties and a consideration of overdensity sizes. Structures can be missed either if slices are too narrow - when associated galaxies are not grouped together - or if slices are excessively wide, which results in a decrease in overdensity signal. Similar to previous work, slices of 7.5 pMpc in depth are used ($\delta z \sim 0.036$ at $z = 3.35$) with an oversampling factor of $10\times$.

We perform 100 Monte Carlo (MC) iterations, in which the $p(z)$ of every photometric galaxy is resampled to minimize the effect of photometric redshift uncertainties. A statistical treatment of spectroscopic redshifts is also included, in which the quality of the spectroscopic redshift determines how often that redshift is used compared to a draw from that galaxy's $p(z)$ (see Section 3.3 of Le Fèvre et al. 2015). In practice, the spectroscopically targeted galaxies with redshift quality flags of 3 or 4 have their spectroscopic redshift used in 99.4% of all iterations, galaxies with redshift quality flags 2 or 9 have their spectroscopic redshift used in 70.0% of all iterations, and galaxies with redshift quality flags 0 or 1 do not have their spectroscopic redshifts used at all. In such iterations where the spectroscopic redshift is not used, the redshift of a galaxy is determined via a draw from the galaxy's $p(z)$.

For each of the 100 iterations, Voronoi tesselation is performed in each redshift slice. The results are then regridded onto a regular grid of size 75×75 kpc, with the median density at a location in all iterations assigned to each voxel, $\Sigma_{VMC,\alpha,\delta,z}$.

3.1.2 Overdensity maps

The typical density of the universe evolves with time, and thus we are more concerned with the relative overdensity of a galaxy's environment rather than a pure density value. This is calculated by normalizing each density in a redshift slice by the median density of all voxels in the map at the same redshift, $\log(1 + \delta_{\mathrm{VMC},\alpha,\delta,z}) = \log(1 + \Sigma_{\mathrm{VMC},\alpha,\delta,z}/\bar{\Sigma}_{\mathrm{VMC},z})$. Additionally, given the extended nature of high-redshift protoclusters, the possibility exists that the entire field may be over- or underdense in a particular redshift slice, which could bias our overdensity calculations. To account for this, we fit a Gaussian to the distribution of $\log(1 + \delta_{\mathrm{VMC},\alpha,\delta,z})$ values in each redshift slice, to obtain the average and variance of the overdensity values therein (see Figure 1). A 5$^{\mathrm{th}}$-order polynomial is then fit to the average overdensities as a function of redshift, removing any effects of field-filling over- or underdensities and obtaining a smoothed overdensity distribution, $\log(1 + \delta_{f^5,\alpha,\delta,z})$. We note that the differences between these two measures of overdensity, $\log(1 + \delta_{\mathrm{VMC},\alpha,\delta,z})$ and $\log(1 + \delta_{f^5,\alpha,\delta,z})$, are on the order of several parts in one thousand, which is $\sim 10\times$ smaller than the spread of values at a given redshift, and thus does not have a significant effect on our results.

Finally, the overdensity of a galaxy $\log(1 + \delta_{\mathrm{gal}})$ is simply the fit overdensity value $\log(1 + \delta_{f^5,\alpha,\delta,z})$ of the voxel which contains the galaxy's three-dimensional position in space in a given iteration. We also calculate the z-score of a galaxy's overdensity value, σ_δ, using the fit median and standard deviation values at the redshift of interest. This value will be the primary overdensity metric used in this work.

3.2 Structure Identification

As described in Cucciati et al. (2018); Shen et al. (2021), we identify overdense structures by finding all contiguous voxels with $\sigma_\delta > 2$ (> 5 for peak regions). The volume enclosed within these envelopes can then be converted to a total mass based on the average comoving matter density and average overdensity of voxels within the envelope. Following this process, a set of coeval structures with enclosed masses $\log(M_{\mathrm{tot}}/\mathrm{M}_\odot) \gtrsim 14$ in close proximity at $3.20 < z < 3.45$ were identified in Forrest et al. (2023). While that work focused on characterization of the structures themselves, in this work we analyze the galaxy populations therein. In both cases, an accurate determination of the extent and overdensity of these structures is critical to understanding the effects such environments have on their component galaxies.

3.2.1 Effects of Uneven Spectroscopic Sampling

To this end, analyzing the dependence of overdensity strength of a region on spectroscopic completeness is a critical test. Using the above VMC method, a real overdensity with all members spectroscopically confirmed will have a stronger signal (higher σ_δ) than the same overdensity with no spectroscopically confirmed members as the latter will have the total signal spread out in redshift space due to the width of the $p(z)$. Alternatively, if a region has little to no spectroscopically confirmed galaxies, it is possible that the VMC data may identify an overdensity when none is truly there. This requires that the $p(z)$ distributions of many galaxies in a small projected area overlap significantly in redshift space.

We attempt to quantify these effects by looking at the spatial variance of: 1) the spectroscopic sampling rate (SSR) - the number of galaxies photometrically within some volume which have been
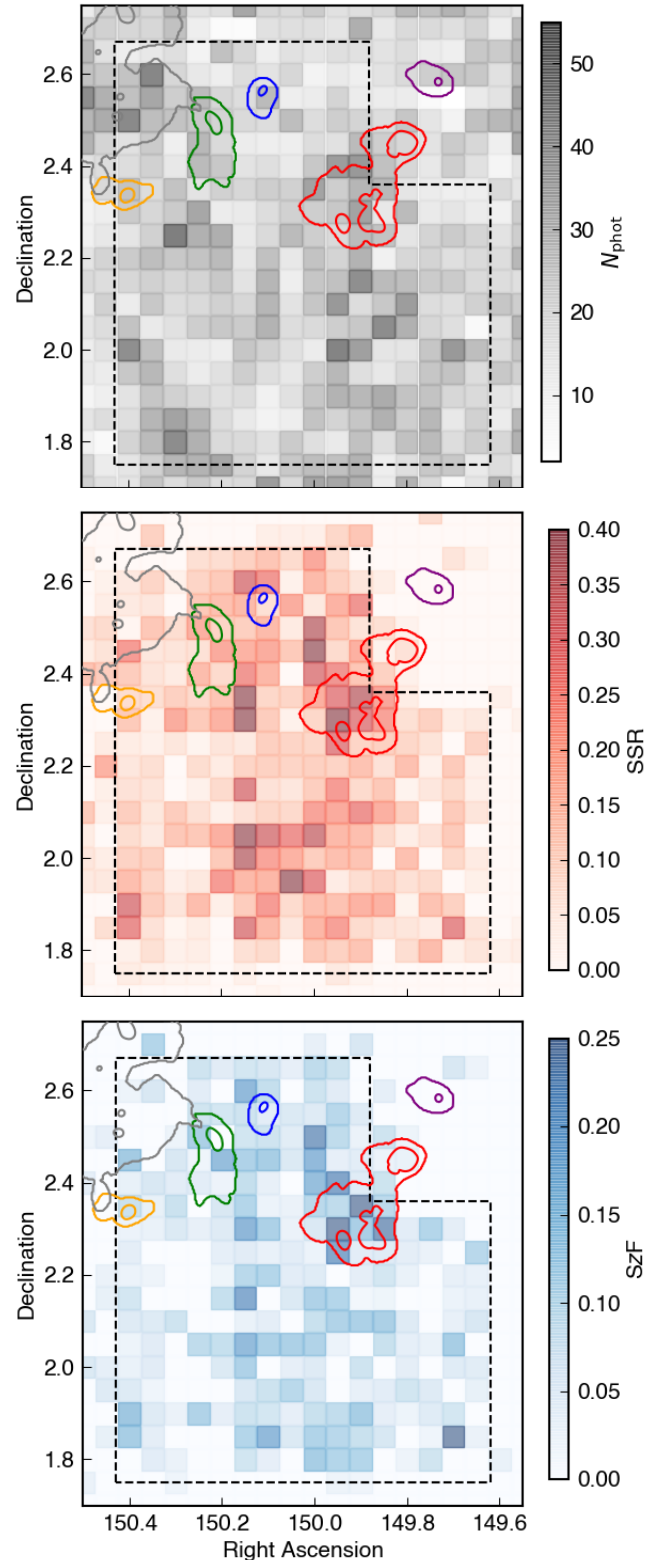

Figure 2. The relative numbers of photometric and spectroscopic galaxies in COSMOS in $3'\times3'$ bins across $3.0 < z < 3.7$ near the VUDS footprint. **Top:** The number of galaxies from the COSMOS2020 catalog in $3'\times3'$ bins with photometric redshifts $3.0 < z < 3.7$. The structures associated with Elentári (Forrest et al. 2023) are shown as contours representing 2σ and 5σ overdensities collapsed over $3.0 < z < 3.7$. **Middle:** Similar to the top panel, but showing the spectroscopic sampling rate. **Bottom:** Similar to the top panel, but showing the spectroscopic redshift fraction.

spectroscopically targeted divided by the total number of galaxies with a photometric redshift within that same volume, and 2) the spectroscopic redshift fraction (SzF), which we define here as the number of galaxies which have a confirmed spectroscopic redshift within some volume divided by the number of galaxies with a photometric redshift within that same volume. We calculate these fractions in spatial bins of $3' \times 3'$ over the full $3.0 < z < 3.7$ redshift range considered for Elentári and the associated field. This is shown in Figure 2 along with the number of objects with photometric redshifts in each bin.

As can be seen in the bottom two panels of Figure 2, the SSR and SzF both fall off significantly outside of the VUDS footprint (dashed line) while the number of photometric targets stays roughly constant across the same boundary (top panel). Overdensities identified in regions with low SzF have an increased probability of being false detections as the signal may be dominated by broad photometric redshift probability distributions, *e.g.,* S6 from Forrest et al. (2023), shown by the very extended gray contour. However, some regions with low SzF may still be real if there are significant spectroscopic confirmations, *e.g.,* the extension of S1 from Forrest et al. (2023) (red contours) outside of the VUDS footprint. This particular region has 14 confirmed spectroscopic members from targeted follow-up with MAGAZ3NE (McConachie et al. 2022). Clearly, further spectroscopic observations of potential overdensities in such regions can resolve this issue.

The possibility also exists that overdensities identified in regions with high SzF and SSR, while real, are less overdense in reality than the VMC maps would suggest. We address this issue with data in hand by ignoring the spectroscopic redshifts of some galaxies and rerunning the analysis. Indeed, removing all C3VO and MAGAZ3NE spectroscopy from our sample limits the effects of intentional spectroscopic targeting of regions of interest. Rerunning the VMC mapping and overdensity detection in this manner produces the results shown in Figure 3, where new structure overdensity contours of $+2\sigma$ and $+5\sigma$ are shown as filled cyan and magenta regions, respectively, and the original Elentári overdensities as reported in Forrest et al. (2023) are shown as open colored contours.

Commonly identified structures differ by medians of $78''$ in projection and 0.002 in redshift. However, this can be split into those structures mostly within the VUDS footprint (S2 - orange contour on Fig. 3 - and S3 in green) with projected offsets of $8.1''$ and $22''$ and those which extend outside (S1 in red and S6 in gray) with projected offsets of $133''$ and $160''$. For the former two structures the two maps result in volume differences of 8.0% and 0.7% and mass differences of 0.04 dex and 0.01 dex, in remarkable agreement. The overdensity-weighted central three-dimensional locations for commonly identified peaks differ in the two cases by similar amounts, with median differences of $18''$ in projection and 0.002 in redshift. Noting that the typical systematic uncertainty for determining the stellar mass of a galaxy at similar epochs is estimated to be ~ 0.2 dex (Mobasher et al. 2015; Leja et al. 2019), we feel that the characterization of these structures' masses and positions is robust to the effects of targeted spectroscopic followup at the levels obtained. Regions extending beyond the VUDS outline without significant additional spectroscopy are difficult to characterize accurately however.

3.3 The Stellar Mass Function

In order to investigate environmental effects on galaxy evolution, we construct stellar mass functions (SMFs) based on the overden-
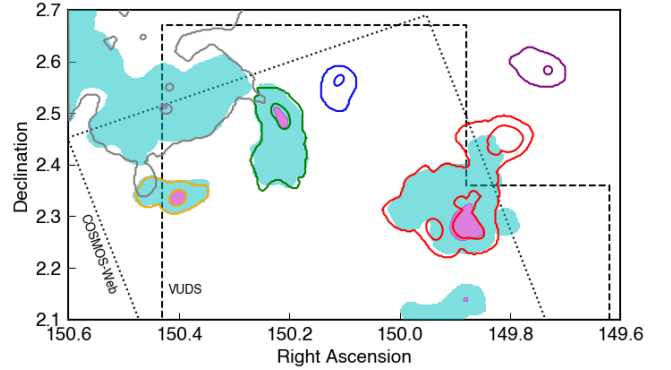

Figure 3. The recovery of overdensities in the field of interest with (empty colored contours at $+2\sigma$ and $+5\sigma$) and without (filled cyan and magenta contours at $+2\sigma$ and $+5\sigma$) targeted follow-up spectroscopy. The former set are as presented in Forrest et al. (2023).

sities derived from the VMC maps. Similar to the generation of the VMC maps, we run 100 realizations drawing from the $p(z)$ of galaxies without reliable spectroscopic redshifts and determine the significance of the overdensity in which each galaxy resides, σ_δ, from the VMC map at the redshift in the realization. All galaxies are subsequently refit using LePhare using the same methodology as when refitting the spectroscopically confirmed galaxies, but instead using the redshifts drawn from the $p(z)$. The resultant galaxy stellar masses are then used to construct SMFs. The volume associated with a SMF is the volume of the VMC map within the associated redshift and σ_δ cuts.

For each realization, SMFs are constructed over $3.20 < z < 3.45$ from galaxies in bins of σ_δ: $-5 < \sigma_\delta < 2$ (field), $2 < \sigma_\delta < 3$, $3 < \sigma_\delta < 4$, and $\sigma_\delta > 4$. There are insufficient galaxies at $\sigma_\delta > 5$ to recover a SMF in this regime with enough signal-to-noise to make significant conclusions, and the same is true for using galaxies within each structure of Elentári separately. Consistent results are found from constructing a combined SMF for all galaxies in all regions of Elentári and from calculating the SMF based on overdensity values of $\log(1 + \delta_{gal})$ as well. We confirm that the field SMF is insensitive to other possible definitions, for example averaging galaxies with $-5 < \sigma_\delta < 2$ at $3.0 < z < 3.2$ and $3.5 < z < 3.7$ and that the field SMF is also in very good agreement with those over $3 < z_{phot} < 4$ based on the COSMOS2015 (Davidzon et al. 2017) and COSMOS2020 (Weaver et al. 2023) catalogs.

The median SMFs in each overdensity bin from all realizations are shown in Figure 4, with error bars representing the 16th-84th percentile range. In addition to the vertical offset that is a result of the selected regions being overdense, a difference in the shape of the SMFs is also apparent and can be seen in Figure 5, in which the ratio of each SMF with that of the field is displayed. In all overdense regions, there is a trend of increasingly elevated SMF relative to the field with increasing stellar mass, and regions of greater overdensity show a stronger trend, a pattern also seen in lower redshift cluster SMFs (Tomczak et al. 2017; van der Burg et al. 2020). This higher ratio of high-mass to low-mass galaxies in overdense regions is consistent with galaxies in protocluster environments undergoing, or having previously undergone, increased mass build-up relative to field galaxies.
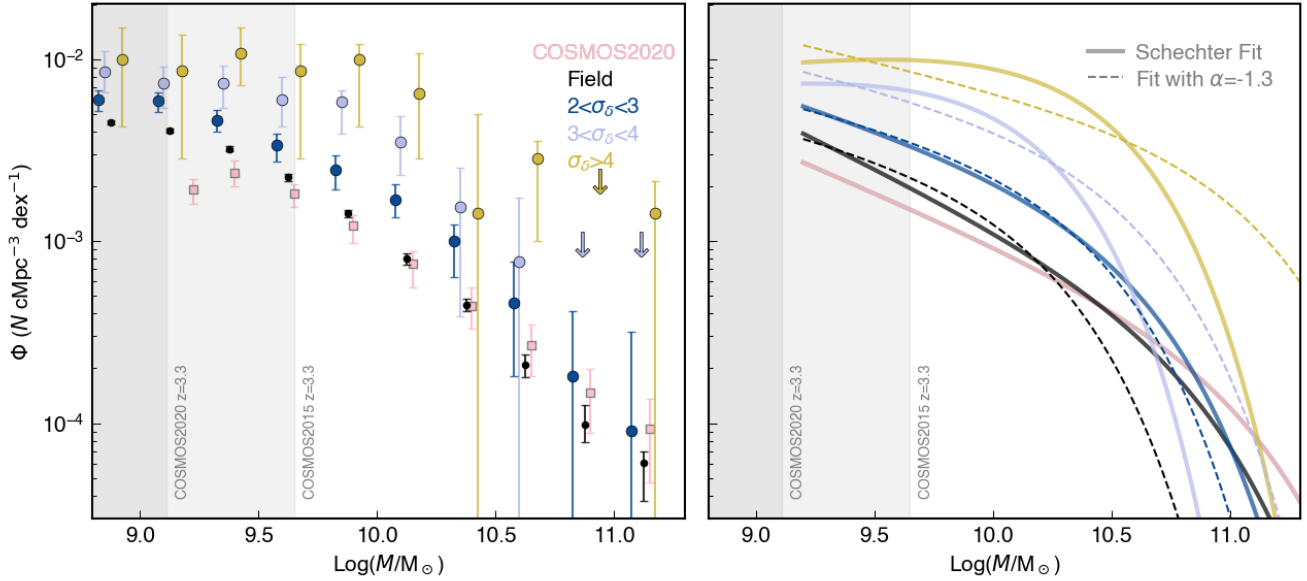
We compare our results to those from the $z \sim 1$ ORELSE

Figure 4. The stellar mass function in several bins of overdensity at $3.20 < z < 3.45$. **Left:** The SMF of the field from COSMOS2020 over $3.0 < z < 3.5$ (**?**) is shown as a series of pink squares, while the field as measured in this work is shown as a series of black points. The SMFs of galaxies in bins of $2 < \sigma_\delta < 3$, $3 < \sigma_\delta < 4$, and $\sigma_\delta > 4$ are shown as blue, periwinkle, and gold points, respectively. Error bars from this work represent the range of 16th to 84th percentiles from MC iterations added in quadrature to Poisson noise. Note that this does not include uncertainty due to cosmic variance, which is the dominant source of error in the COSMOS2020 analysis, and thus the error bars between the two works should not be compared. Masses below the stellar mass completeness limits at $z = 3.3$ for the COSMOS2015 and COSMOS2020 catalogs are shaded. **Right:** The best-fit Schechter function to each measured SMF is shown as a solid line with the same color scheme. Another fit to each SMF performed fixing α=-1.3 is shown as a dashed curve.

survey (Tomczak et al. 2017) which used a similar methodology for determination of overdensity. The qualitative trends seen in the $z \sim 1$ cluster sample are similar to those in this work, with the ratio of high-mass to low-mass galaxies increasing with increasing overdensity. Additionally, as shown in Figure 5, when converting our SMFs from σ_δ to $\log(1 + \delta_{\rm gal})$ we find that the SMF for galaxies at similar overdensities appears the same at both $z \sim 1$ and $z \sim 3.3$. This is consistent with the hypothesis that group environments are host to evolutionary effects (*e.g.,* mergers) which 'pre-process' galaxies before their eventual residence in cluster environments (Zabludoff et al. 1996; McGee et al. 2009; Bahé et al. 2019).

Additionally, we fit a single-Schechter function (Schechter 1976) to each SMF, first allowing the pivot mass (M^*), faint-end slope (α), and normalization (ϕ^*) parameters to vary, and then again fixing $\alpha = -1.3$. The best-fit parameterizations are given in Table 3. We compare the pivot mass and faint-end slope values to those from studies of $z \sim 1$ cluster SMFs (Tomczak et al. 2017; van der Burg et al. 2020) shown in Figure 6. In general, we find that the pivot mass decreases and the faint-end slope becomes shallower with increasing overdensity. This is perhaps not so much due to the average galaxy mass decreasing (the term 'characteristic mass' is sometimes used for M^*), but is instead a result of environmental processes increasing the number of galaxies around or just below this mass. This increase may be due to increased merger rates in overdense environments (Tomczak et al. 2017) or increased numbers of quiescent galaxies (Nantais et al. 2016; van der Burg et al. 2020).

3.4 Quiescent Fractions

The fraction of galaxies with SFRs below the main sequence of star formation (*i.e.,* quenched) at a given epoch is significantly increased

Table 3. The parameters of Schechter function fits to the SMFs at varying densities. The best-fit values for varying $M*$, α, and $\phi*$ are shown as are the results for fixing $\alpha = 1.3$.

Density bin	$\log(M^*/M_\odot)$	α	$\phi^*/(10^{-3}\ \mathrm{Mpc}^{-3})$
$\sigma_\delta < 2$	10.86±0.10	-1.63±0.04	0.16±0.04
	10.20±0.05	=-1.3	0.87±0.07
$2 < \sigma_\delta < 3$	10.58±0.03	-1.42±0.01	0.66±0.04
	10.40±0.03	=-1.3	1.07±0.05
$3 < \sigma_\delta < 4$	10.08±0.10	-0.86±0.09	4.83±0.78
	10.58±0.19	=-1.3±	1.49±0.33
$\sigma_\delta > 4$	10.38±0.14	-0.86±0.17	6.57±2.00
	11.10±0.20	=-1.3	1.40±0.35

in cluster environments relative to the coeval field out to $z \gtrsim 1$ (Van Der Burg et al. 2013; Tomczak et al. 2017; van der Burg et al. 2020). High-redshift protocluster environments at $z \gtrsim 2$ do not generally show these same quenched fractions, though some counterexamples appear to exist, at least with regards to high mass galaxies (Chartab et al. 2020; Shi et al. 2021; Ito et al. 2023), which has been seen in one of the peaks of Elentári (McConachie et al. 2022). Analyzing how the SMFs of such quenched galaxies vary relative to the field environments can help uncover the mechanisms responsible for accelerated evolution of galaxies in overdense systems (Tomczak et al. 2017; Papovich et al. 2018, *e.g.,*).

For each of the 100 $p(z)$ sampling realizations, we calculate the number of quiescent and star-forming galaxies over $3.20 < z < 3.45$ in two ways. First, we use the popular comparison of $U - V$ and $V - J$ rest-frame colors (*e.g.,* Williams et al. 2009; Muzzin et al. 2013; Straatman et al. 2016) as modeled by LePhare and
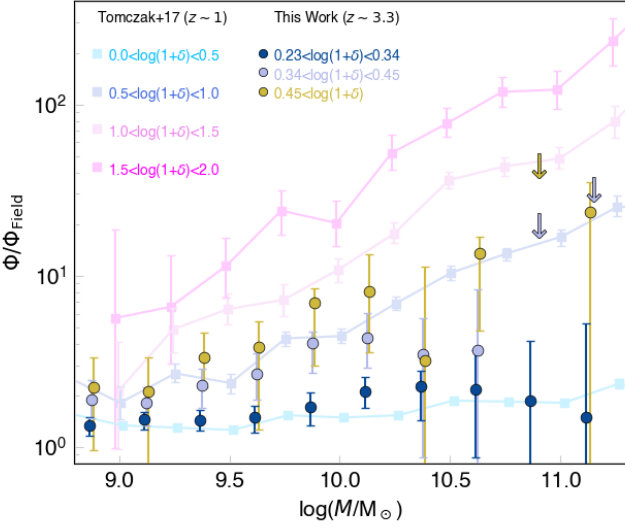
Figure 5. The ratio of the stellar mass function at different overdensities to that observed in the field. The gold, periwinkle, and blue points are as in Fig. 4 and represent galaxies in regions with overdensities of roughly $0.23 < \log(1+\delta) < 0.34$, $0.34 < \log(1+\delta) < 0.45$, and $\log(1+\delta) > 0.45$ at $z \sim 3.3$. Similar points from Tomczak et al. (2017) at $z \sim 1$ are shown for comparion. SMFs of similar overdensity seem to scale to the field in similar manners at both redshifts.

the wedge location specified for $2.0 < z < 3.5$ from Whitaker et al. (2011). We also fit the relation between SFR as as function of stellar mass (Daddi et al. 2007; Salmon et al. 2015, *e.g.,*) by finding the median SFR in overlapping bins of width 0.2 dex with centers separated by 0.01 dex, smoothing via a first-order Savitzsky-Golay filter, and fitting with a quadratic polynomial. Galaxies with SFRs more than 1 dex below this 'star-forming main sequence' (SFMS) are then considered quiescent. The resultant numbers of galaxies with $\log(M_*/M_\odot) > 9.1$, the mass completeness of the COSMOS2020 Classic catalog at this redshift, are given in Table 4.

While the numbers of identified quiescent galaxies in the overdense regions are too small to construct SMFs from, we can compute quiescent fractions, which we plot in the right panel of Figure **??**, along with quiescent/star-forming selections for an example MC iteration in the left and middle panels. No statistically significant differences between field and overdense environments are seen, though the uncertainties are significant. The two methodologies also seem to be in general agreement, with the UVJ color selection identifying more quiescent galaxies then the SFMS cut, particularly for galaxies with $\log(M_*/M_\odot) < 10$.

We do note however, that while the COSMOS2020 photometric catalog is complete down to $\log(M_*/M_\odot) \sim 9.1$ at $z \sim 3.3$, most of the spectroscopy used for construction of the VMC maps is biased toward the detection of star-forming galaxies, which may artificially inflate the quenched fractions seen here. The follow-up observations with MOSFIRE are less sensitive to this bias, but still no enhancement in quenched fraction relative to the field is seen in the overdense environments which were targeted with MOSFIRE.

3.5 Relations between Stellar Mass, Age, and Overdensity

Observed increases in the masses of galaxies residing in overdense environment relative to the field population could be caused by
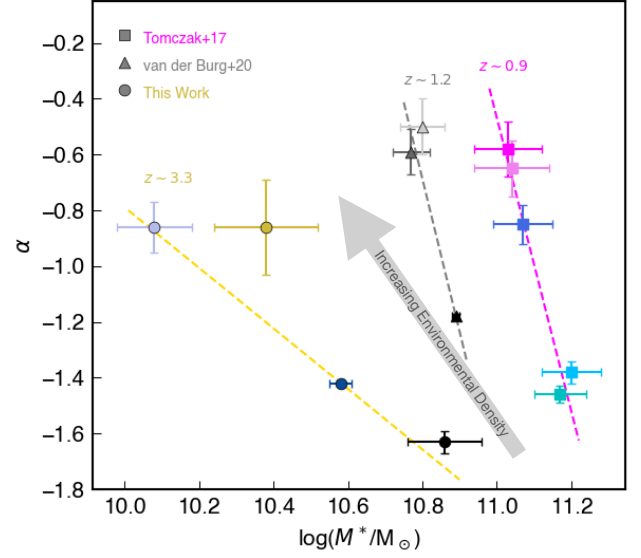

Figure 6. Comparison of the pivot mass (M^*) and faint-end slope (α) fit values from studies of the SMF in overdense environments. Values from this work are shown as circles of the same colors as in Fig. 4, values from $z \sim 1.2$ GOGREEN clusters van der Burg et al. (2020) are grayscale triangles, and values from $z \sim 0.9$ ORELSE clusters Tomczak et al. (2017) are cyan to magenta. A simple weighted linear fit each dataset is shown in gold, gray, and magenta, respectively.

Table 4. The number of quiescent galaxies and the associated quenched fractions in the field and overdensity samples across $3.20 < z < 3.45$ identified using UVJ colors and sSFR. Results only considering galaxies with masses $\log(M_*/M_\odot) > 9.1$ and $\log(M_*/M_\odot) > 10.0$ are both shown.

	$UVJ_{M>9.1}$	$UVJ_{M>10}$	$SFMS_{M>9.1}$	$SFMS_{M>10}$
$N_{SF,field}$	$3593.0^{+129.0}_{-137.0}$	$463.0^{+37.0}_{-38.0}$	$3688.0^{+131.0}_{-136.0}$	$477.0^{+39.0}_{-36.0}$
$N_{Q,field}$	$130.0^{+40.0}_{-29.0}$	$50.0^{+23.0}_{-14.0}$	$37.0^{+17.0}_{-12.0}$	$37.0^{+15.0}_{-12.0}$
$N_{SF,od}$	$398.0^{+81.0}_{-71.1}$	$61.5^{+24.0}_{-22.1}$	$398.0^{+88.6}_{-65.1}$	$59.0^{+29.0}_{-18.9}$
$N_{Q,od}$	$7.5^{+13.8}_{-7.1}$	$4.0^{+6.3}_{-4.0}$	$2.0^{+5.4}_{-1.7}$	$2.0^{+5.4}_{-1.7}$
QF_{field}	$3.49^{+1.07}_{-0.78}$	$9.75^{+4.48}_{-2.73}$	$0.99^{+0.46}_{-0.32}$	$7.20^{+2.92}_{-2.33}$
QF_{od}	$1.85^{+3.40}_{-1.74}$	$6.11^{+9.66}_{-6.11}$	$0.50^{+1.34}_{-0.43}$	$3.28^{+8.77}_{-2.84}$

factors such as enhanced star formation rates due to gas inflows or bursts of star formation as a result of increased merger rates. Depending on when these effects occur, it is possible that the ages of galaxies of a given mass will have a dependence upon their environment. While in theory stellar ages can be discerned from spectral absorption features and the shape of the SED, the spectra of the vast majority of sources in this work do not have the requisite signal to noise to measure ages precisely, having spectral detections of emission lines only. In an attempt to discern age differences between the field and structure populations, we fit the photometry of each spectroscopically-confirmed galaxy with the redshift fixed to the spectroscopic redshift using the `LePhare` (Arnouts et al. 1999; Ilbert et al. 2006) and FAST++ (Schreiber et al. 2018) programs. We then compare the stellar mass and age derived from these fits to the σ_δ of each galaxy and perform a Spearman correlation test (Figure 8).

As seen in the SMF analysis, we find a weak ($\rho = 0.105$), though significant ($p = 0.008$) correlation between massive galaxies and overdense environments. A commonly found correlation between stellar mass and age is also recovered ($\rho = 0.476$,
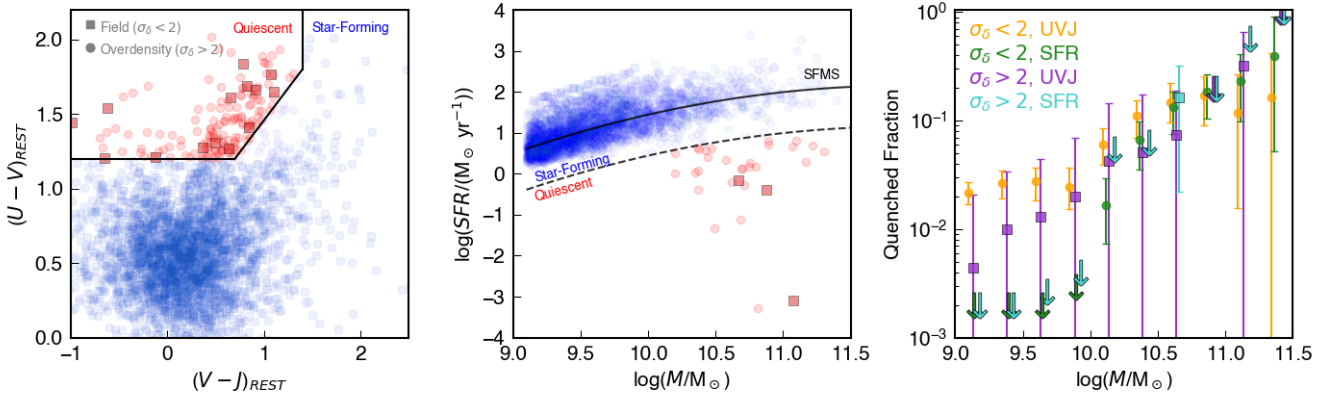
Figure 7. The identification of star-forming and quiescent galaxies at $3.20 < z < 3.45$. **Left:** The restframe UVJ color-color plane for a single MC iteration. Red symbols above/left of the dividing wedge are considered quiescent, with squares indicating those galaxies in overdense environments and circles indicating galaxies in the field. Blue symbols below/right of the dividing wedge are classified as star-forming. **Center:** The SFR-stellar mass plane for a single MC iteration. The solid black curve is the median relation termed the star-forming main sequence (SFMS), while the dashed curve is 1 dex below the SFMS and is used to distinguish between star-forming and quiescent galaxies. The symbol colors and shapes remain the same. **Right:** The quenched fraction as a function of stellar mass averaged over all 100 MC iterations. Orange circles represent the field quenched fraction identified using the UVJ selection. Green circles represent the field quenched fraction identified using the SFMS selection. Purple squares represent the field quenched fraction identified using the UVJ selection. Turquoise squares represent the field quenched fraction identified using the SFMS selection. Downward-facing arrows indicate upper limits. While an increasing trend with stellar mass is seen, the sample sizes are insufficient to distinguish between the quenched fractions in field and overdense environments.
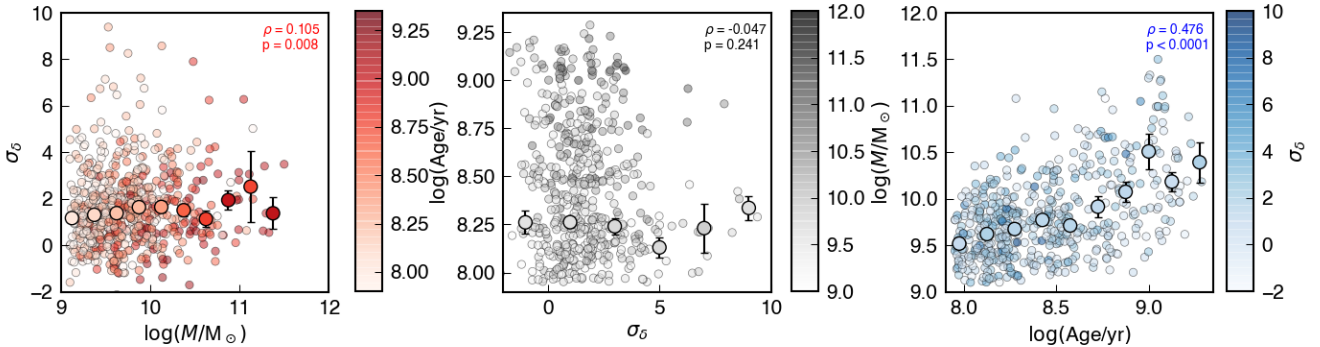

Figure 8. Comparison of stellar mass, stellar age, and environmental overdensity from SED fitting for spectroscopically confirmed galaxies at $3.0 < z < 3.7$ in COSMOS shown in three different projections. Median values are shown by the large circles, with the error bars representing the uncertainty on the calculated median. The Spearman ρ coefficient and p-value are shown in each panel for the set of parameters on the ordinate and abcissa.

$p < 0.0001$). However, there is no significant trend for this sample between age and overdensity. This could indicate that gas-rich mergers which trigger bursts of star formation are not responsible for the increased stellar masses of galaxies in these overdense environments. It should be noted though that age determinations from SED fitting have significant uncertainties as well as degeneracies with stellar mass and dust extinction (*e.g.,* Mobasher et al. 2015), and thus drawing strong conclusions from these tests is not supported.

4 CONCLUSIONS

In this work we construct and compare stellar mass functions and quiescent fractions in several bins of environmental overdensity in the COSMOS field centered on the Elentári overdensity at $z \sim 3.35$. Such an analysis is only possible at these epochs with the extensive

amounts of photometry and spectroscopy available in well-studied fields such as COSMOS. These are used to build a three-dimensional density map to accurately estimate the environmental density field in which a galaxy resides and consider in this work galaxies above the approximate stellar mass completeness of the COSMOS2020 catalog at $z \sim 3.3$, $\log(M_*/\mathrm{M_\odot}) \sim 9.1$.

We observe distinct shapes of the stellar mass function between galaxies in overdense environments and galaxies in the field at $3.20 < z < 3.45$, with the densest regions having number densities $\sim 6\times$ that of the field for galaxies with $\log(M_*/\mathrm{M_\odot}) \sim 10.0$, compared to only $\sim 3\times$ that of the field for galaxies with $\log(M_*/\mathrm{M_\odot}) \sim 9.5$. This distinction clearly indicates that the environment in which a galaxy resides begins to have an effect on its evolution prior to the galaxy entering a cluster environment. The increased number of high mass galaxies in dense environments is suggestive of the long-theorized 'pre-processing' (Balogh et al.

2000; De Lucia et al. 2012; Donnari et al. 2020), in which the masses of such galaxies are enhanced in proto-cluster or even group systems via mergers and/or increased *in situ* SFRs before infall into proper clusters, eventually resulting in the quenching of star formation in these overdense systems before quenching in field galaxies. However, the quiescent fractions of galaxies in field and overdense environments do not differ, peaking at $\sim 20-30\%$ for galaxies with $\log(M_*/M_\odot) \sim 11.0$ suggesting that while processes of mass enhancement in overdense environments have begun, processes which enhance the quenched fraction in these same environments have not yet had significant effects.

Finally, we compare the relationship between stellar mass, stellar age, and environmental overdensity of spectroscopically-confirmed galaxies. We find statistically significant positive correlations between stellar mass and stellar age, as well as between stellar mass and environmental overdensity. This again suggests that while the overdense structure of Elentári may be affecting the evolution of member galaxies through enhanced mass growth, there does not appear to be enhanced quenching of member galaxies. Further observations, particularly of the densest protocluster cores in Elentári are

REFERENCES

Aihara H., et al., 2019, Publications of the Astronomical Society of Japan, 71, 1

Annunziatella M., et al., 2014, Astronomy and Astrophysics, 571

Annunziatella M., et al., 2016, Astronomy and Astrophysics, 585, 1

Arnouts S., Cristiani S., Moscardini L., Matarrese S., Lucchin F., Fontana A., Giallongo E., 1999, Monthly Notices of the Royal Astronomical Society, 310, 540

Ashby M. L., et al., 2013, Astrophysical Journal, 769

Ashby M. L., et al., 2015, Astrophysical Journal, Supplement Series, 218, 33

Ashby M. L. N., et al., 2018, The Astrophysical Journal Supplement Series, 237, 39

Bahé Y. M., et al., 2019, Monthly Notices of the Royal Astronomical Society, 485, 2287

Balogh M. L., Navarro J. F., Morris S. L., 2000, The Astrophysical Journal, 540, 113

Balogh M. L., et al., 2017, Monthly Notices of the Royal Astronomical Society, 470, 4168

Balogh M. L., et al., 2020, Monthly Notices of the Royal Astronomical Society, 31, 1

Blanton M. R., Moustakas J., 2009, Annual Review of Astronomy and Astrophysics, 47, 159

Bruzual G., Charlot S., 2003, Monthly Notices of the Royal Astronomical Society, 344, 1000

Calzetti D., Armus L., Bohlin R. C., Kinney A. L., Koornneef J., Storchi-Bergmann T., 2000, The Astrophysical Journal, 533, 682

Capak P. L., et al., 2011, eprint arXiv:1101.3586, pp 1–16

Chabrier G., 2003, Publications of the Astronomical Society of the Pacific, 115, 763

Chartab N., et al., 2020, The Astrophysical Journal, 890, 7

Chiang Y.-K., Overzier R. A., Gebhardt K., Henriques B., 2017, The Astrophysical Journal, 844, L23

Cooper M. C., Newman J. A., Davis M., Finkbeiner D. P., Gerke B. F., 2012, spec2d: DEEP2 DEIMOS Spectral Pipeline, https://ascl.net/1203.003

Cucciati O., et al., 2014, Astronomy and Astrophysics, 570, 1

Cucciati O., et al., 2018, Astronomy & Astrophysics, 619, A49

Daddi E., et al., 2007, The Astrophysical Journal, 670, 156

Davidzon I., et al., 2017, Astronomy and Astrophysics, 605

De Lucia G., Weinmann S., Poggianti B. M., Aragón-Salamanca A., Zaritsky D., 2012, Monthly Notices of the Royal Astronomical Society, 423, 1277

Donnari M., et al., 2020, Monthly Notices of the Royal Astronomical Society, 500, 4004

Dressler A., 1984, The Astrophysical Journal, 281, 512

Faber S. M., et al., 2003, Instrument Design and Performance for Optical/Infrared Ground-based Telescopes, 4841, 1657

Fitzpatrick E. L., Massa D., 1986, The Astrophysical Journal, 307, 286

Forrest B., et al., 2017, The Astrophysical Journal, 838, L12

Forrest B., et al., 2020, The Astrophysical Journal, 903, 47

Forrest B., et al., 2023, Monthly Notices of the Royal Astronomical Society: Letters, 526, L56

Fumagalli M., Krumholz M. R., Prochaska J. X., Gavazzi G., Boselli A., 2009, Astrophysical Journal, 697, 1811

Hasinger G., et al., 2018, The Astrophysical Journal, 858, 77

Hatch N. A., Kurk J. D., Pentericci L., Venemans B. P., Kuiper E., Miley G. K., Röttgering H. J., 2011, Monthly Notices of the Royal Astronomical Society, 415, 2993

Horne K., 1986, Publications of the Astronomical Society of the Pacific, 98, 609

Hung D., et al., 2020, Monthly Notices of the Royal Astronomical Society, 491, 5524

Hutchison T., Walawender J., Kwok S., 2020,] 10.1117/12.2562864, p. 114

Ilbert O., et al., 2006, Astronomy and Astrophysics, 457, 841

Ilbert O., et al., 2009, The Astrophysical Journal, 690, 1236

Ilbert O., et al., 2013, Astronomy and Astrophysics, 556, 1

Ito K., et al., 2023, The Astrophysical Journal Letters, 945, L9

Kauffmann G., White S. D., Heckman T. M., Ménard B., Brinchmann J., Charlot S., Tremonti C., Brinkmann J., 2004, Monthly Notices of the Royal Astronomical Society, 353, 713

Kawinwanichakij L., et al., 2017, The Astrophysical Journal, 847, 134

Koekemoer A. M., et al., 2007, The Astrophysical Journal Supplement Series, 172, 196

Kriek M., et al., 2015, The Astrophysical Journal Supplement Series, 218, 1

Laigle C., et al., 2016, The Astrophysical Journal Supplement Series, 224, 24

Le Fèvre O., et al., 2003, Instrument Design and Performance for Optical/Infrared Ground-based Telescopes, 4841, 1670

Le Fèvre O., et al., 2013, Astronomy and Astrophysics, 559

Le Fèvre O., et al., 2015, Astronomy & Astrophysics, 576, A79

Leauthaud A., et al., 2007, The Astrophysical Journal Supplement Series, 172, 219

Leja J., et al., 2019, The Astrophysical Journal, 877, 140

Lemaux B. C., et al., 2014, Astronomy and Astrophysics, 572, 1

Lemaux B. C., Tomczak A. R., Lubin L. M., Wu P-F., Gal R. R., Rumbaugh N., Kocevski D. D., Squires G. K., 2017, Monthly Notices of the Royal Astronomical Society, 472, 419

Lemaux B. C., et al., 2018, Astronomy & Astrophysics, 615, A77

Lemaux B. C., et al., 2019, Monthly Notices of the Royal Astronomical Society, 490, 1231

Lemaux B. C., et al., 2022, Astronomy & Astrophysics, 662, A33

Lilly S. J., et al., 2007, The Astrophysical Journal Supplement Series, 172, 70

Lubin L. M., Gal R. R., Lemaux B. C., Kocevski D. D., Squires G. K., 2009, Astronomical Journal, 137, 4867

Marchesini D., Van Dokkum P. G., Förster Schreiber N. M., Franx M., Labbé I., Wuyts S., 2009, Astrophysical Journal, 701, 1765

Marsan Z. C., et al., 2022, The Astrophysical Journal, 924, 25

McConachie I., et al., 2022, The Astrophysical Journal, 926, 37

McCracken H. J., et al., 2012, Astronomy & Astrophysics, 544, A156

McGee S. L., Balogh M. L., Bower R. G., Font A. S., McCarthy I. G., 2009, Monthly Notices of the Royal Astronomical Society, 400, 937

McLean I. S., et al., 2010, in McLean I. S., Ramsay S. K., Takami H., eds, Vol. 7735, Ground-based and Airborne Instrumentation for Astronomy III. p. 77351E, doi:10.1117/12.856715, http://proceedings.spiedigitallibrary.org/proceeding.aspx?doi=10.1117/12.856715

McLean I. S., et al., 2012, in McLean I. S., Ramsay S. K., Takami H., eds, Vol. 8446, Ground-based and Airborne Instrumentation for Astronomy IV. , doi:10.1117/12.924794,

http://proceedings.spiedigitallibrary.org/proceeding.aspx?doi=10.1117/12.924794

Mobasher B., et al., 2015, Astrophysical Journal, 808

Moneti A., et al., 2019, ESO Science Archive Facillity - Phase 3 Data Release Description, pp 1–15

Muldrew S. I., Hatch N. A., Cooke E. A., 2015, Monthly Notices of the Royal Astronomical Society, 452, 2528

Muzzin A., et al., 2012, Astrophysical Journal, 746

Muzzin A., et al., 2013, The Astrophysical Journal Supplement Series, 206, 8

Nantais J. B., et al., 2016, Astronomy & Astrophysics, 592, A161

Newman J. A., et al., 2013, Astrophysical Journal, Supplement Series, 208

Noble A. G., et al., 2018

Oke J. B., Gunn J. E., 1983, The Astrophysical Journal, 266, 713

Onodera M., et al., 2012, Astrophysical Journal, 755

Papovich C., et al., 2018, The Astrophysical Journal, 854, 30

Peng Y.-j., et al., 2010, The Astrophysical Journal, 721, 193

Pickles A., 1998, Publications of the Astronomical Society of the Pacific, 110, 863

Polletta M., et al., 2007, The Astrophysical Journal, 663, 81

Prevot M. L., Lequeux J., Prevot L., Maurice E., Rocca-Volmerange B., 1984, Astronomy and Astrophysics, 132, 389

Salmon B., et al., 2015, The Astrophysical Journal, 799, 183

Sawicki M., et al., 2019, Monthly Notices of the Royal Astronomical Society, 489, 5202

Schechter P., 1976, The Astrophysical Journal, 203, 297

Schreiber C., et al., 2018, Astronomy & Astrophysics, 611, A22

Scoville N., et al., 2007, The Astrophysical Journal Supplement Series, 172, 1

Shah E. A., et al., 2023, 10, 1

Shen L., et al., 2021, The Astrophysical Journal, 912, 60

Shi K., Toshikawa J., Lee K.-S., Wang T., Cai Z., Fang T., 2021, The Astrophysical Journal, 911, 46

Stefanon M., et al., 2015, The Astrophysical Journal, 803, 11

Steinhardt C. L., et al., 2014, Astrophysical Journal Letters, 791, 6

Straatman C. M. S., et al., 2016, pp 1–36

Taniguchi Y., et al., 2007, The Astrophysical Journal Supplement Series, 172, 9

Taniguchi Y., et al., 2015, Publications of the Astronomical Society of Japan, 67, 1

Thomas D., Maraston C., Bender R., de Oliveira C. M., 2005, The Astrophysical Journal, 621, 673

Tomczak A. R., et al., 2017, Monthly Notices of the Royal Astronomical Society, 472, 3512

Tran K.-V. H., et al., 2010, The Astrophysical Journal, 719, L126

Van Der Burg R. F., et al., 2013, Astronomy and Astrophysics, 557, 1

Wang T., et al., 2016, The Astrophysical Journal, 828, 56

Weaver J. R., et al., 2022, The Astrophysical Journal Supplement Series, 258, 11

Weaver J. R., et al., 2023, Astronomy & Astrophysics, 677, A184

Whitaker K. E., et al., 2011, The Astrophysical Journal, 735, 86

Williams R. J., Quadri R. F., Franx M., van Dokkum P., Labbé I., 2009, The Astrophysical Journal, 691, 1879

Zabludoff A. I., Zaritsky D., Lin H., Tucker D., Hashimoto Y., Shectman S. A., Oemler A., Kirshner R. P., 1996, The Astrophysical Journal, 466, 104

Zamojski M. A., et al., 2007, The Astrophysical Journal Supplement Series, 172, 468

van der Burg R. F. J., et al., 2020, Astronomy & Astrophysics, 638, A112

APPENDIX A: OBJECT MATCHING

We use observations of galaxies from the zCOSMOS (Lilly et al. 2007), VUDS (Le Fèvre et al. 2015), and DEIMOS10k (Hasinger et al. 2018) spectroscopic surveys, as well as observations taken with Keck/MOSFIRE as part of the C3VO (Lemaux et al. 2022) and MAGAZ3NE (Forrest et al. 2020) surveys to construct a master spectroscopic catalog. The targets in these samples are drawn from various observational catalogs in the COSMOS field and here we detail the process of matching these observations to galaxies in the COSMOS2020 photometric catalog (Weaver et al. 2022).

A1 Astrometric Correction

For each spectroscopic survey, each spectroscopic entry (s_i) is matched to the nearest photometric catalog member (p_{j0}) in projected space. The coordinates for spectroscopic entries are then updated based on the median positional offsets between the data sets, median($\Delta\alpha_{i,j0}$) and median($\Delta\delta_{i,j0}$), providing a first-order astrometric correction. These median offsets are $\lesssim 0.1''$ arcseconds in all cases.

A2 Positional Threshold

Catalog matching is performed again to find the nearest photometric catalog member (p_j). We then use the distribution of distances between matches to calculate our matching tolerance, considering that this distribution is composed of a combination of correct matches and random nearest matches in cases where the spectroscopic target is not in the photometric catalog. These two components become clear by analyzing the histogram of logarithmic distance separations (Figure A1).

We fit a Gaussian to each of these distributions and take the 3σ upper limit for the main peak (assumed to be correct matches) to be the distance threshold within which to search for a given spectroscopic survey. Alternatively taking the 3σ limit from fitting a single Gaussian to the entire distribution or by choosing the distance at which the contribution of the two Gaussians are equal, while changing the number of galaxies matched, does not result in differences to the scientific conclusions of this work. For objects in the VUDS, C3VO, zCOSMOS, and DEIMOS10k surveys, this search radius threshold is 0.70", 0.53", 0.49", and 1.35", respectively, which successfully matches 91.0%, 94.2%, 95.0%, and 92.7% of entries.

A3 Single Matches

If there is a single photometric match to a spectroscopic object within the 3σ radius threshold of a survey, we take the two entries to be matches to the same object.

A4 Multiple Matches

Many of the spectroscopic entries in the catalog have more than one photometric catalog member which satisfies both the distance and magnitude threshold cuts above. In these cases, comparisons are also made between the spectroscopic redshift and the photometric redshifts of potential matches, as well as differences in their total i- and K-band magnitudes, resulting in a four-parameter comparison. If no other spectroscopically-confirmed galaxies are nearby, the photometric member with the better weighted combination of values is determined to be the correct match. If another spectroscopic entry is also nearby, the photometric and spectroscopic entries are paired based on closest positional match.
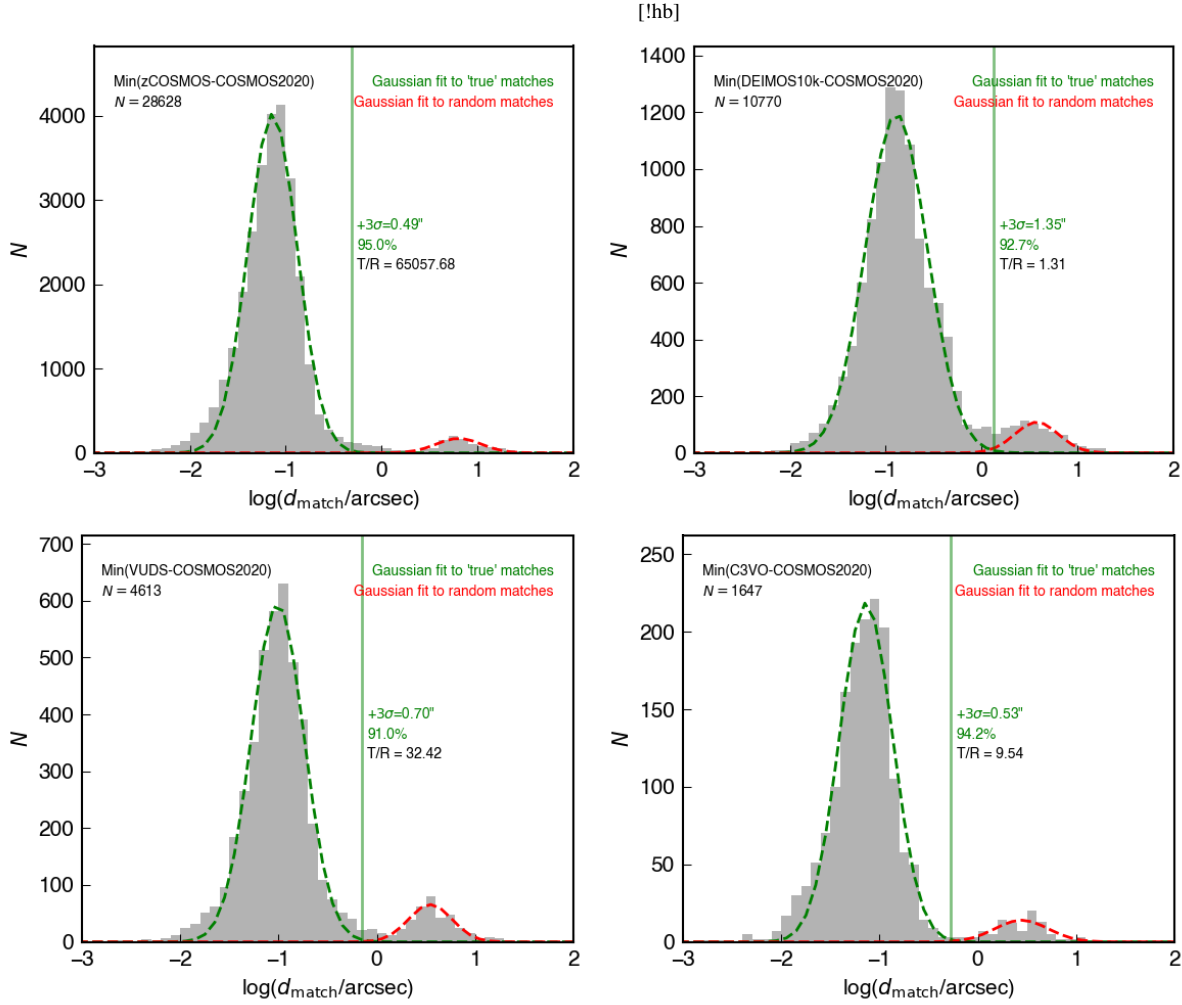
[!hb]

Figure A1. Determination of matching thresholds. **Left:** The distribution of distances from each spectroscopic object to the nearest photometric catalog member. **Right:** The distribution of differences in K-band magnitude from each spectroscopic object to the nearest photometric catalog member.

A5 No Matches

There are 2237 spectroscopic entries in the catalog which have no photometric catalog members that satisfy the distance threshold cuts above. These objects are retained in the final spectroscopic catalog and are considered when generating the VMC maps, however they are not included in further analyses which require determination of stellar mass, SFR, etc. as they do not have the requisite photometry for performing SED fitting.

A6 Duplicates

At this point, each spectroscopic object is considered to be matched to the correct photometric catalog object. As such, photometric catalog objects with multiple spectroscopic matches exist and are given a true multi-spec flag. If these spectroscopic entries (which have a quality flag of 3, 4, or 9) have the same redshift, this is considered the spectroscopic redshift. When discrepant spectroscopic redshifts with good quality flags exist, the instrument and survey are used to determine the correct redshift. In order of priority, these are: C3VO, MAGAZ3NE, VUDS, DEIMOS-10k, zCOSMOS (updated catalog), zCOSMOS (original catalog).

This paper has been typeset from a TEX/LATEX file prepared by the author.